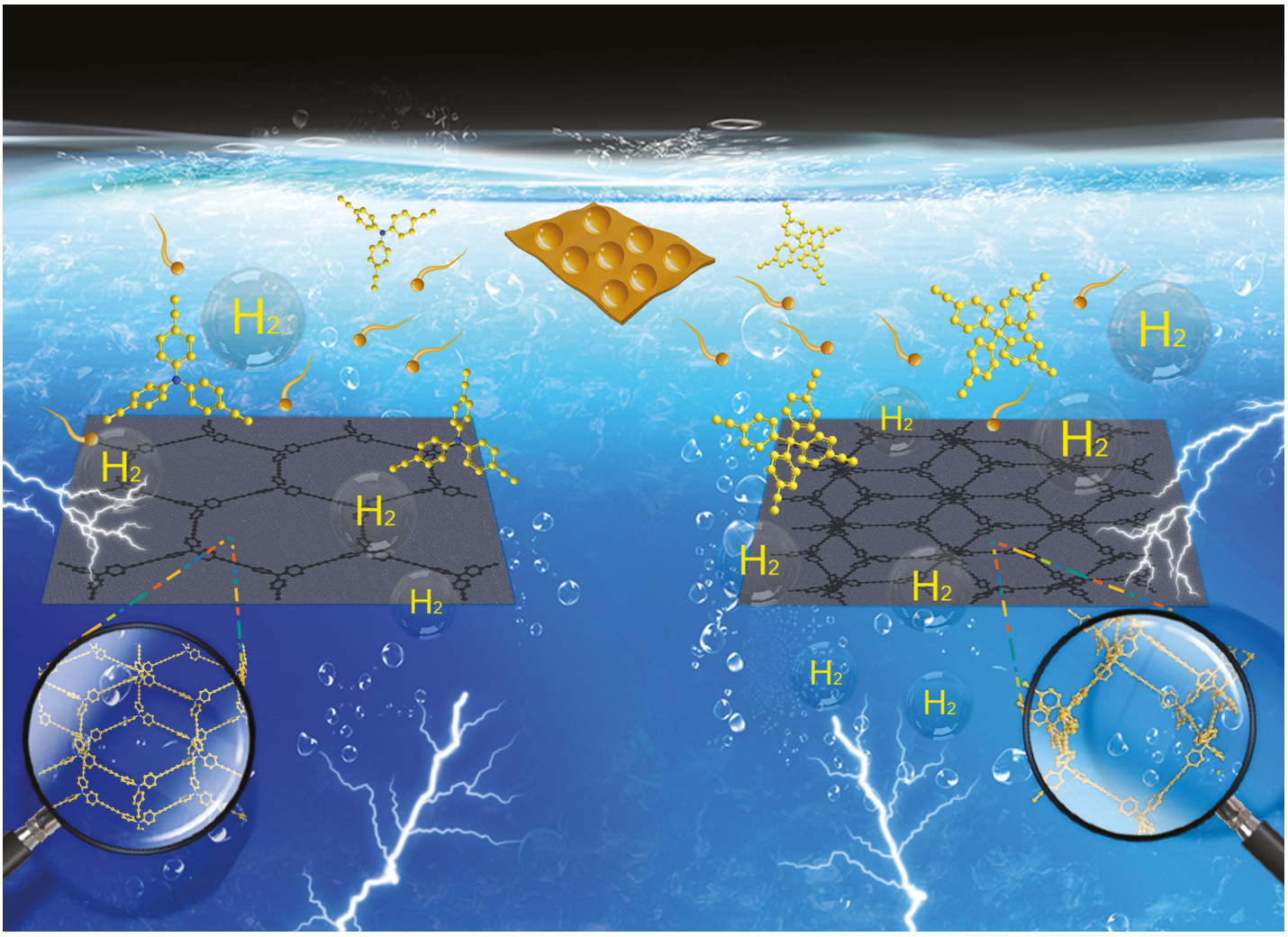

Showcasing research from Professor Ning Wang *et al.* from Science Center for Material Creation and Energy Conversion, Shandong University

Acetylenic bond-driven efficient hydrogen production of a graphdiyne based catalyst

Tetraphenyl methane substitute graphdiyne (TPM-GDY) and triphenyl amine substitute graphdiyne (TPN-GDY) are prepared through bottom-to-top synthetic strategy. 3D acetylenic bond distribution makes porous TPM-GDY film have a larger number of active sites, which plays a key role in the excellent performance of TPM-GDY in hydrogen evolution reaction.

As featured in:

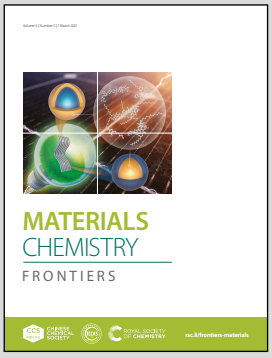

See Ning Wang *et al.*,
Mater. Chem. Front., 2021, **5**, 2247.

MATERIALS CHEMISTRY FRONTIERS

RESEARCH ARTICLE

View Article Online
View Journal | View Issue

Cite this: *Mater. Chem. Front.*, 2021, **5**, 2247

Acetylenic bond-driven efficient hydrogen production of a graphdiyne based catalyst†

Ling Bai,[a] Zhiqiang Zheng,[a] Zhongqiang Wang,[a] Feng He,[b] Yurui Xue[a] and Ning Wang *[a]

Received 12th January 2021,
Accepted 7th February 2021

DOI: 10.1039/d1qm00064k

rsc.li/frontiers-materials

The presence of acetylenic bonds in graphdiyne (GDY) endow this type of carbon allotrope with high intrinsic catalytic activity, which is significantly superior to traditional carbon materials. Here, a synthetic strategy has been developed to study the influence of active acetylenic bond ratio and spatial distribution on the hydrogen evolution reaction (HER) catalytic performance. Two kinds of GDY, namely tetraphenylmethane-graphdiyne (TPM-GDY) and triphenylamine-graphdiyne (TPN-GDY), have been rationally synthesized *via* a bottom-to-up synthetic strategy. From the structural view, both TPM-GDY and TPN-GDY possess the 1,4-diphenylbuta-1,3-diyne skeleton composed of electrocatalytic active sp carbon. TPM-GDY possesses more active sp carbon exposed to the surface than TPN-GDY, which makes the TPM-GDY electrode exhibit better HER performance. Besides, some other properties of GDY-based carbon materials such as morphology, surface area, and pore distribution can also be efficiently adjusted. The above-mentioned results indicate that the distribution of active sites in the carbon framework plays a critical role in improving the catalytic performances, which offers a new strategy for creating highly active and stable electrocatalysts.

Introduction

Carbon materials have been widely applied in electrochemical catalytic reactions and have shown bright perspectives due to the advantages of extensive resources, diverse architectures, low toxicity, lightness, and excellent chemical durability.[1–6] Nevertheless, carbon-based electrocatalysts also suffer from inferior activity in contrast to expensive noble metal catalysts.[7–9] To solve this bottleneck, numerous efforts have been made to generate more number of active sites on carbon materials, including heteroatom doping, transition metal incorporating, and defect engineering.[10–19] The above-mentioned strategies are mainly focused on changing the intrinsic structure and conjugation of the carbon allotropes, which would trigger the charge density redistribution of carbon. As a result, more active sites for catalytic reaction could be generated adjacent to the induced heteroatoms or the contact interface between carbon and hybrid loading materials. However, the harsh preparation conditions and the introduction of other heteroatom elements would inevitably result in undetermined structures and weaken the advantage of the carbon material. On the other hand, the catalytic reaction occurs at the interface between the catalyst surface and the electrolyte solution. The effective number of active sites that can indeed participate in the electrochemical catalytic processes is another key factor affecting the catalytic activity. Therefore, involving more active sites in the catalytic reaction is another pathway that is worthy of being explored. Typically, the morphology and size regulation of carbon-based nanomaterials are important strategies to enlarge the active area, create more active sites and thus improve electrochemical catalytic performances.[20–22]

Graphdiyne (GDY) is a single layer of sp- and sp^2-hybridized all carbon network,[23–26] in which each benzene ring (sp^2 carbon) is uniformly linked by six butadiyne units (sp carbon), inducing extremely uneven surface charge distribution and thus imparting GDY with high intrinsic catalytic activity.[27–30] Besides, the large natural pores in GDY guarantees the extra in-plane transfer tunnels for either ions or even small organic molecules in the perpendicular direction to the GDY carbon networks.[31] The above unique structural features of GDY make it an excellent candidate for conventional catalysts. For instance, recent studies indicate that GDY-supported electrocatalysts such as single metal atom-anchored GDY,[32] GDY-supported $NiCo_2S_4$,[33] and N-doped GDY supported MoS_2 nanosheets[34] have shown high hydrogen evolution performance and stability. Another superiority of GDY is that it can be prepared *via* a synthetic chemical method under mild conditions, which provides us a facile way to realize the structural

[a] *Science Center for Material Creation and Energy Conversion, School of Chemistry and Chemical Engineering, Institute of Frontier and Interdisciplinary Science, Shandong University, Jinan 250100, P. R. China. E-mail: wang_ning@sdu.edu.cn*
[b] *Key Laboratory of Organic Solids, Institute of Chemistry, Chinese Academy of Sciences, Beijing 100190, P. R. China*

† Electronic supplementary information (ESI) available. See DOI: 10.1039/d1qm00064k

modification on the premise of not destroying the intrinsic and conjugated structure of GDY.[35,36] Recently, a series of heteroatom-doped GDY materials such as fluorine-doped GDY,[37] pyrazine type GDY[38] and pyridine nitrogen-doped GDY[39] have been prepared *via* a bottom-to-up strategy, and have also shown excellent electrocatalytic performance. Moreover, a broad and precise platform to investigate the structure activity relationship of carbon electrochemical catalysts has also been fabricated. All the above-mentioned studies indicate that the electrochemical active sites on GDY originate from the existence of quantitative acetylenic bonds (sp carbon) throughout the whole carbon framework. Thus, the effective utilization of these acetylenic bonds should be a key issue to further improve the catalytic performance of GDY-based materials.

Inspired by such outstanding and unique properties of GDY, herein, we construct a platform to investigate the structure–activity relationships while the amount of active acetylenic groups in GDY can be adjusted. Tetraphenylmethane-based GDY (TPM-GDY) is prepared through the bottom-to-up synthetic strategy. As shown in Fig. 1a, TPM-GDY owns a three-dimensional (3D) carbon framework composed of homogeneously-distributed sp^3 hybridized carbon and adjacent 1,4-diphenylbuta-1,3-diyne linkers. Compared to the reference triphenylamine-based GDY (TPN-GDY) with a two-dimensional (2D) structure (Fig. 1b), TPM-GDY owns more amount of alkynyl groups exposed on the surface, which can take part in the electrochemical process occurring at the interface between the GDY based electrode and electrolyte. Moreover, TPM-GDY grown on the carbon cloth (CC) shows an ordered aggregation structure with high surface area and multi-scale pore size distribution, which effectively increases the contact area of the TPM-GDY based electrode. The electrochemical test confirms that the 3D acetylenic growth strategy can efficiently maximize the electrochemical active sites of the catalyst, which induces the excellent performance of the TPM-GDY-based electrode in hydrogen evolution reaction (HER).

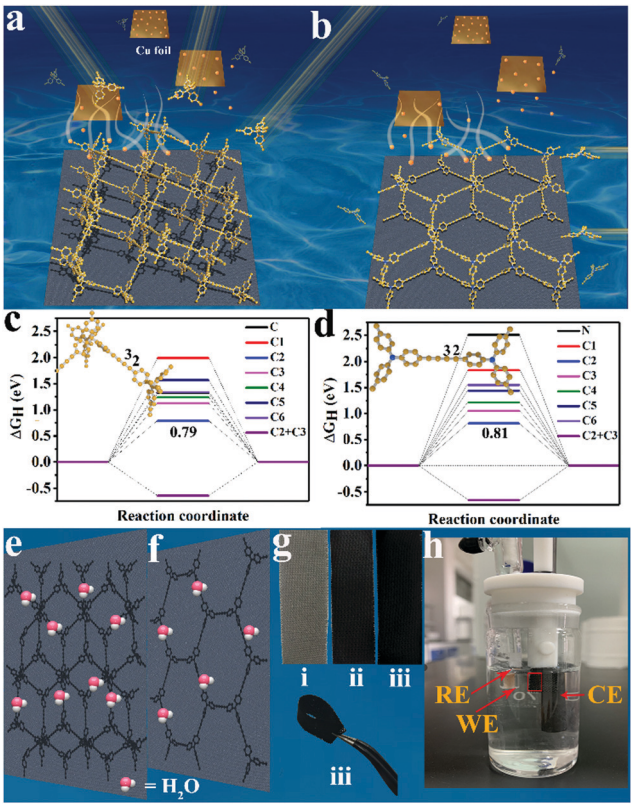

Fig. 1 Schematic for the cross-coupling process of TPM-GDY (a) and TPN-GDY (b) on CC substrates. The yellow and blue balls represent the carbon and nitrogen atoms, respectively. The calculated free energy (ΔGH) on different carbon atoms of (c) TPM-GDY and (d) TPN-GDY. C2 and C3 represent the carbon atoms in the acetyl groups adjacent and away from the benzene ring, respectively. The inset images show the selected repeating units. C1, C4, C5, and C6 represent the carbon atoms on the benzene ring. C represents the sp^3 carbon in TPM-GDY; N represents the nitrogen atoms in TPN-GDY. Illustration of the acetylenic active bonds distributing on the surface layer of TPM-GDY/CC (e) and TPN-GDY/CC (f) based working electrodes, which can effectively interact with H_2O molecules. (g) The photographs of blank CC (i), TPN-GDY/CC (ii), and TPM/CC (iii). (h) The photograph of a three-electrode electrolysis cell for HER, in which WE, RE, and CE represent the working, reference, and counter electrodes, respectively.

Results and discussion

Design and synthesis

The TPM-GDY and TPN-GDY films grown on CC were prepared *via* the modified Glaser–Hay coupling reaction.[40] The copper foils were put in the reaction solvent to act as the copper-ion-catalyst supplier (Fig. 1a and 1b). Tetrakis(4-ethynylphenyl)methane and tris(4-ethynylphenyl)amine were used as precursors, which were synthesized *via* a typical Sonogashira reaction starting from tetrakis(4-bromophenyl)methane and tris(4-bromophenyl)amine, respectively (Scheme S1, ESI†).[41] The structures of the precursors were fully characterized with ^{1}H NMR and ^{13}C NMR spectra (Fig. S2, ESI†). During the coupling process, the precursors were added to the reaction solvent slowly and transferred to the surface of the CC substrate together with copper ions exfoliated from copper substrates. Notably, the different orientations of alkynyl groups in the two precursors determine the different configurations of corresponding GDY analogues. In detail, the as-prepared TPM-GDY possessed a 3D GDY such as a carbon framework, in which sp^3 hybridized central carbon atoms and four 1,4-diphenylbuta-1,3-diyne linkers composed of sp-hybridized carbons were evenly distributed. The tetrakis(4-ethynylphenyl)methane precursors can continuously couple to the reactive sites of acetylene groups to form the TPM-GDY framework (Fig. S1, ESI†). This 3D acetylene constructing strategy is suitable for fabricating GDY analogues with a stereoscopic configuration. On the other hand, TPN-GDY is a 2D carbon framework composed of central nitrogen heteroatoms and three 1,4-diphenylbuta-1,3-diyne linkers (Fig. 1b). We examine the numerous possible active sites in TPM-GDY (Fig. 1c) and TPN-GDY (Fig. 1d) for catalyzing hydrogen evolution in an acidic condition based on DFT calculations.[42] The corresponding H adsorption configurations are shown in Fig. S3 (ESI†). By utilizing the computational hydrogen electrode (CHE) model, it is found that the hydrogen adsorption free energy on the C2 site in both TPM-GDY and TPN-GDY are 0.79 and 0.81 eV, respectively.

This result indicates that the C2 atom in the acetylenic bond is the most favourable active site in TPM and TPN. It should be noted that the hydrogen adsorption free energy on the sp^3 carbon in TPM-GDY and heteroatom nitrogen in TPN-GDY are calculated to be 1.32 and 2.50 eV, respectively. This result confirms that the function of the sp^3 carbon and heteroatom nitrogen is to only act as a linker for the 1,4-diphenylbuta-1,3-diyne skeleton. Moreover, no catalytic activity is exhibited in these two linker atoms, which made the butadiyne groups in TPM-GDY and TPN-GDY show similar catalytic activity. Besides, the intrinsic activity of the structure and the performance of the TPM-GDY- and TPN-GDY-based electrodes in HER is highly related to the effective active sites that can be exposed to the electrochemical catalytic reaction interface. Based on the theoretically optimized configurations, the 3D carbon framework maximizes the number of active acetylenic bonds on the surface of TPM-GDY films (Fig. 1e and f).[37] Therefore, TPM-GDY/CC is supposed to show higher catalytic activity towards HER. The photograph of the TPM-GDY and TPN-GDY films on the CC substrate (Fig. 1g) reveals that the surface of the bendable electrodes is uniform and continuous. The colour of CC changed from grey to black compared to the pristine one, which can be directly used as working electrodes in HER (Fig. 1h).

Morphology

The morphology of the GDY film grown on CC is an important factor affecting its HER performance.[43] As shown in Fig. 2a and f, the scanning electron microscopy (SEM) images of TPM and TPN films on CC exhibit a uniform morphology. In the case of TPM-GDY, the surface of the film is composed of abundant nanoparticles (Fig. 2b). In the presence of four 1,4-diphenylbuta-1,3-diyne linkages between repeating patterns of sp^3 centre carbon atoms, TPM-GDY features a 3D conjunction, and tends to form nanoparticles (Fig. 2c). Elemental mapping reveals the uniform distribution of the carbon in TPM-GDY (Fig. 2d and e). For TPN-GDY, an aggregation structure morphology is observed in the SEM images (Fig. 2g). The interactions among the adjacent

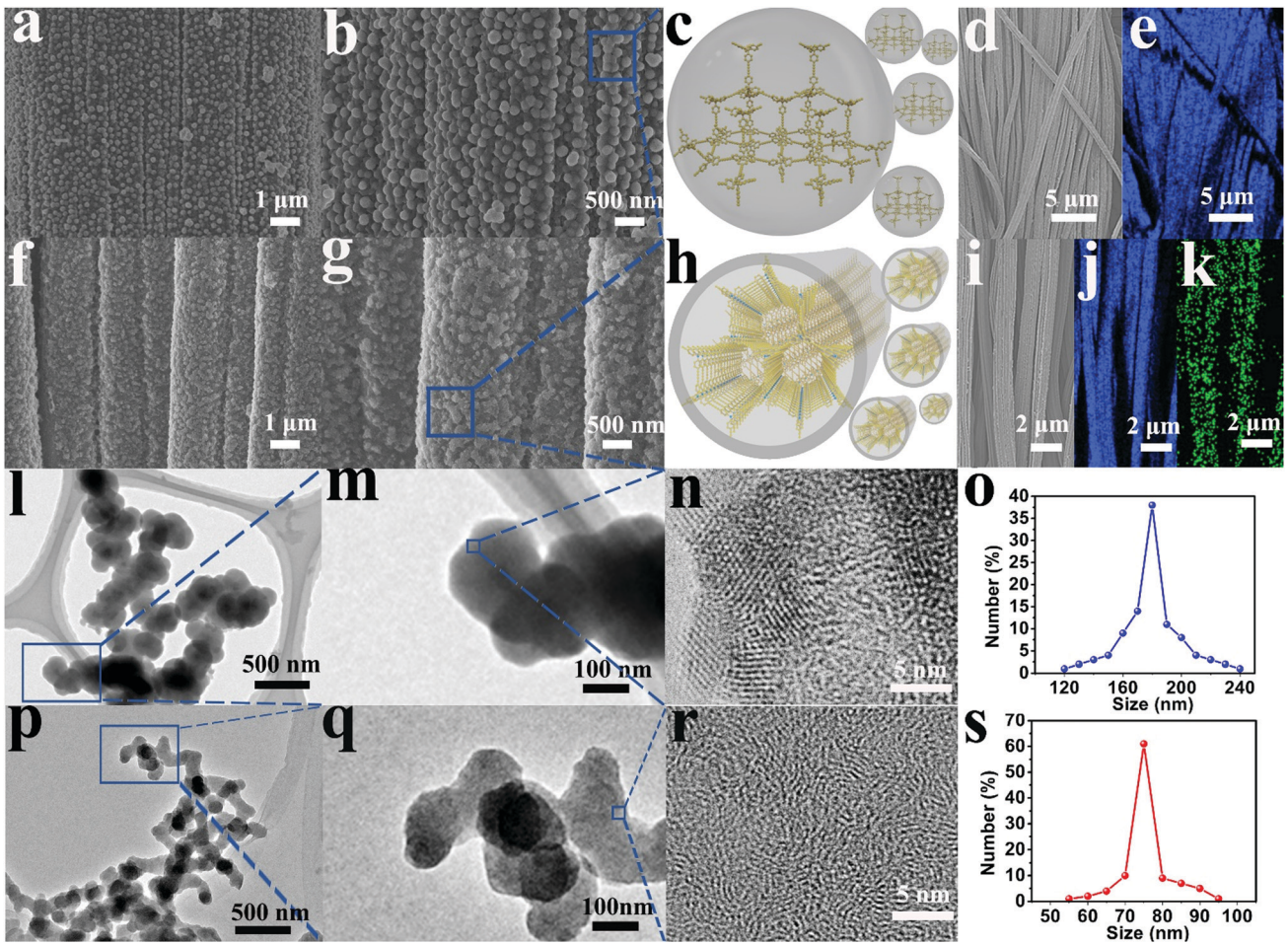

Fig. 2 SEM images of the as-prepared TPM-GDY in large (a) and small (b) scale. (c) The illustration for the aggregation structure of TPM-GDY. SEM image of TPM-GDY film grown on carbon cloth (d) and the corresponding element mapping for carbon (e). SEM images of the as-prepared TPN-GDY in large (f) and small (g) scale. (h) The illustration for the aggregation structure of TPN-GDY. SEM image of TPN-GDY film grown on carbon cloth (i) and the corresponding element mapping for carbon (j) and nitrogen (k). TEM images of TPM film exfoliated from the CC substrate in large (l) and small (m) scale. (n) HRTEM images of TPM-GDY on ultra-thin carbon film. (o) The size distribution of the TPM-GDY aggregation structure. TEM images of TPN film exfoliated from the CC substrate on a large (p) and small (q) scale. (r) HRTEM images of TPN-GDY on ultra-thin carbon film. (s) The size distribution of the TPN-GDY aggregation structure.

layers induces the aggregation of TPN-GDY (Fig. 2h). Elemental mappings indicate the uniform distribution of carbon and nitrogen in TPN-GDY (Fig. 2i–k). Transmission electron microscopy (TEM) images further confirm that the aggregation structure of TPM-GDY is formed by the accumulation of some nanoparticles (Fig. 2l and m), which is consistent with the SEM results. High resolution TEM (HRTEM) images reveal some relative multiple lattice fringes (Fig. 2n). The size distribution of the TPM-GDY aggregation structure is in a range of 120–240 nm (Fig. 2o and Fig. S4, ESI†). In the case of TPN-GDY, the aggregation structure with multiple lattice fringes can be observed in the TEM pictures (Fig. 2p–r). The 3D orientation of acetylenic bonds might provide some connection spots for the growth of the upper layer so that the subsequent precursors can cross-couple to these connection spots continuously and form an ordered adjacent layer in a certain range. Thus, the formation of the regular 3D structure of TPM-GDY can be ascribed to be the 3D orientation of acetylenic bonds in its precursors.[44,45] The size distribution of the TPN-GDY aggregation structure is in a range of 55–95 nm (Fig. 2s and Fig. S5, ESI†). The uniform surface morphology of TPM-GDY/CC and TPN-GDY/CC might be beneficial to involve a more active surface to participate in the HER.[46]

Structural characterization

The bonding environment of carbon atoms with different hybridized types in TPM-GDY is characterized by X-ray photoelectron spectroscopy (XPS) (Fig. S6, ESI†). In detail, the C1s peaks in TPM-GDY can be mainly deconvoluted into five sub-peaks of C–C (sp^2) at 284.4 eV, C–C (sp) at 285.2 eV, C–C (sp^3) at 285.0 eV, C–O at 287.8 eV, and C═O at 289.0 eV, respectively (Fig. 3a). Furthermore, the area ratio of the sp, sp^2, and sp^3 carbon atoms is close to 8 : 24 : 1, consistent with the structure of TPM-GDY. For TPN-GDY, the C1s peaks can also be deconvoluted into five sub-peaks, consisting of C–C (sp^2) at 284.5 eV, C–C (sp) at 285.1 eV, C–N

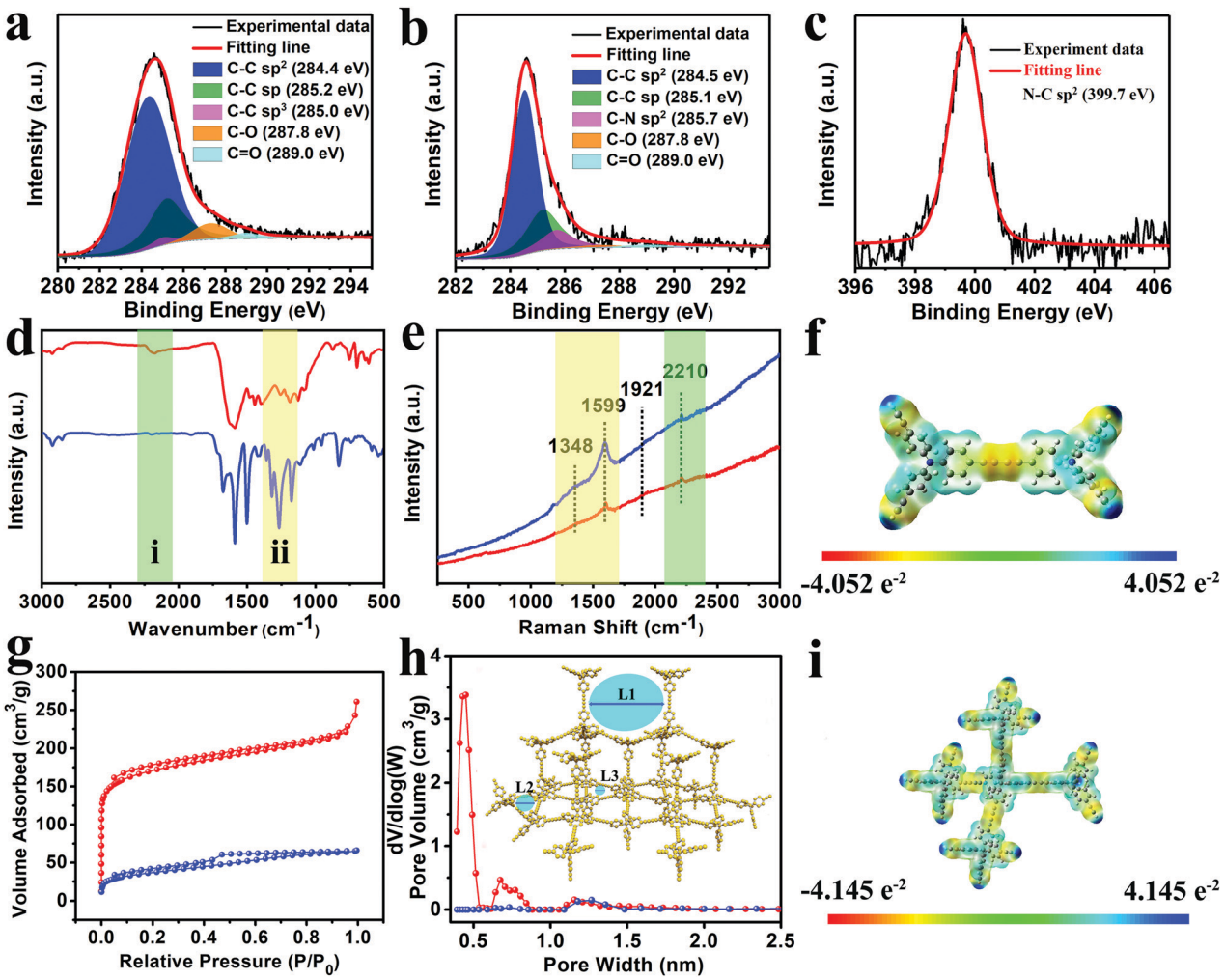

Fig. 3 High-resolution XPS scan for the element carbon in TPM-GDY (a) and TPN-GDY (b). (c) XPS scan for the element nitrogen in TPN-GDY. (d) FTIR spectrum of TPM-GDY and TPN-GDY on CC. (e) Raman spectra of TPM-GDY and TPN-GDY. (f) The calculated electronic distribution on a repeat unit of TPN-GDY. Nitrogen adsorption–desorption isotherm (g) and the corresponding DFT incremental pore size distribution curve (h) for TPM-GDY and TPN-GDY. The inset schematic shows three kinds of pores located at different regions of the 3D TPM-GDY framework. (i) The calculated electronic distribution on a repeat unit of TPM-GDY. The red and blue lines in d, e, g and h represent TPM-GDY and TPN-GDY, respectively.

(sp^2) at 285.7 eV, C–O at 287.8 eV, and C═O at 289.0 eV, respectively (Fig. 3b). The prominent N1s peak at 399.7 eV (Fig. 3c) is assigned to the nitrogen heteroatom linked with three 1,4-diphenylbuta-1,3-diyne groups, indicating the homogeneous bonding environment for the heteroatom nitrogen in the 2D carbon-rich framework. The existence of C═O and C–O groups in the fitting peaks of carbon may be due to the oxygenation of the acetylene group in the margin of the carbon frameworks.[47] The typical functional groups in TPM-GDY and TPN-GDY are characterized *via* Fourier transform infrared spectroscopy (FT-IR) (Fig. 3d). The peaks located in the region i (2140–2240 cm^{-1}) can be assigned to the acetylenic bond in TPM-GDY and TPN-GDY.[48–50] The characteristic peaks at 1261 and 1317 cm^{-1} of ν_{C-N} can be found in the spectrum of TPN-GDY, which indicates the existence of the triphenylamine group.[51] The Raman spectra (Fig. 3e) of both TPM-GDY and TPN-GDY samples exhibit four main peaks. Two peaks at 2210 and 1921 cm^{-1} are ascribed to acetylenic bonds. The peaks at 1599 and 1348 cm^{-1} are assigned to the G and D peak of carbon frameworks.[52]

In order to further investigate the surface areas and pore structures of the samples, nitrogen adsorption–desorption studies are performed. As shown in Fig. 3g, the quantity of nitrogen gas adsorbed in the TPM-GDY powder quickly increases while the value of pressure (P/P_0) is lower than 0.1, indicating the existence of micropores in the adsorption process of nitrogen.[53–56] The continuous adsorption curve of nitrogen shows an H3-type hysteresis loop, which can be attributed to the multi-scale adsorption in mesopores.[57] In the case of TPN-GDY, the increasing amount of the nitrogen gas adsorption in the low pressure region is much lower than that of TPM-GDY, which means a lack of micropores in TPN-GDY. Accordingly, the Brunauer–Emmett–Teller (BET) surface area for TPM-GDY is 562 $m^2\ g^{-1}$, which is higher than that of TPN-GDY (131.4 $m^2\ g^{-1}$). The pore size distributions of TPM-GDY and TPN-GDY samples calculated from the corresponding nitrogen adsorption–desorption isotherms using the density functional theory (DFT) method are shown in Fig. 3h. The main pore size distribution for TPM-GDY is located in the following three regions 0.47–0.54 nm, 0.64–0.86 nm, and 1.09–1.48 nm, which can be assigned to the pores in the 3D stereoscopic structure (L3), near the edge (L2), and at the edge (L1), respectively. As for TPN-GDY, the main pores are distributed in the region of 1.09–1.48 nm. This value is smaller than the calculated size of large pores located at the 2D framework of TPN-GDY (Fig. S7, ESI†), which can be attributed to the mixed, stacked configuration of the 2D TPN-GDY framework.[58–60] Generated from the molecular electronic wavefunction, we further obtain the molecular electrostatic potential (ESP) of TPN-GDY (Fig. 3f) and TPM-GDY (Fig. 3i). It is observed that the sp-hybridized carbon atoms in acetylenic bonds (–C≡C–) are rich in electrons, which should be beneficial for the reduction of protons, thus accelerating the HER catalysis.[61]

HER performance

According to our design strategy, the numbers of active acetylenic bonds on the surface of TPM-GDY/CC are more than those on TPN-GDY/CC. Thus, TPM-GDY/CC should show better performance than TPN-GDY/CC in the HER process. To verify this

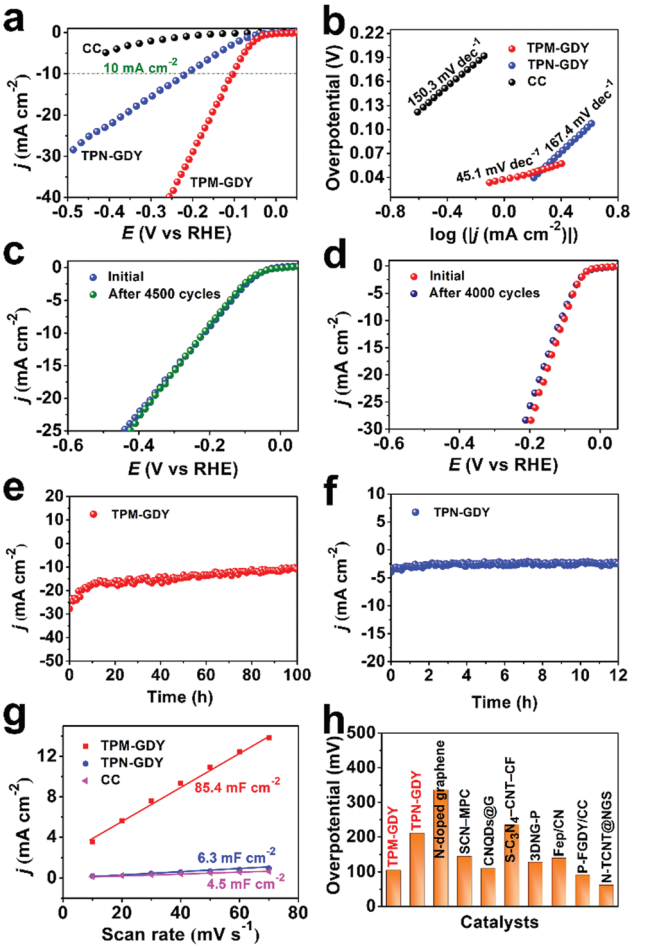

Fig. 4 (a) Polarization curves of TPM-GDY and TPN-GDY for HER in 0.5 M H_2SO_4. (b) Tafel slope for TPM-GDY, TPN-GDY, and CC. (c) Comparison of the initial polarization curves of TPM-GDY after 4500 cycles. (d) Comparison of the initial polarization curves of TPN-GDY after 4000 cycles. Long-term stability tests of TPM-GDY/CC (e) and TPN-GDY/CC (f) in 0.5 M H_2SO_4 during the HER process. (g) Corresponding capacitive current densities as a function of scan rates for CC, TPM-GDY, and TPN-GDY. (h) Comparison of the overpotential for TPM-GDY, TPN-GDY, and reported carbon-based catalysts.

statement, the HER performance of TPM-GDY and TPN-GDY are measured under acidic conditions (0.5 M H_2SO_4). As shown in Fig. 4a, the pure CC shows a negligible catalytic activity. TPM-GDY/CC gives a much smaller overpotential of 105 mV at the current density of 10 mA cm^{-2} than that of TPN-GDY (211 mV) and most of the reported metal-free electrocatalysts (Fig. 4h and Table S1, ESI†). Besides, TPM-GDY/CC exhibits a small Tafel slope of 45.1 mV dec^{-1} compared to that of TPN-GDY/CC (167.4 mV dec^{-1}) (Fig. 4b). These results reveal the higher HER catalytic activity of TPM-GDY than the TPN-GDY sample. Long-term stability is another important parameter for evaluating the performance of the catalyst. TPM-GDY shows no change in current density after 4500 cycles (Fig. 4c), while TPN-GDY exhibits some decrease in the current density only after 4000 cycles (Fig. 4d). This indicates the better stability of TPM-GDY than TPN-GDY. Moreover, there is no decrease in current after

10 h of electrolysis at an applied potential of 120 mV, indicating the good stability of the TPM-GDY/CC- and TPN-GDY/CC-based electrode in HER under strongly acidic conditions (Fig. 4e and f). The active sites on the surface of TPM-GDY and TPN-GDY can also be compared through the experimental measurement of the electrochemical active surface area (ECSA) through the double-layer capacitance method (C_{dl}). As shown in Fig. 4g, TPM-GDY/CC shows a large C_{dl} value (85.4 mF cm^{-2}) compared to that of 2D TPN-GDY film (6.3 mF cm^{-2}) and CC (4.5 mF cm^{-2}). This indicates that 3D acetylene construction in TPM-GDY networks can effectively increase the active surface area and the number of active sites and thus enhance catalytic activity.[62]

Conclusions

In summary, we prepared TPM-GDY and TPN-GDY and compared their performance in HER. TPM-GDY had a high 3D porous structure with repeated units of sp^3 carbon connecting through four 1,4-diphenylbuta-1,3-diyne skeletons. The theoretical calculation result indicates that the HER active sites on both TPM-GDY and TPN-GDY are located at the sp carbon adjacent to the benzene ring. The dense distribution of acetylenic bonds in the TPM-GDY framework makes more active sp carbons participate in the HER process, which occurs on the surface of electrodes. As a result, TPM-GDY shows a low overpotential of 105 mV, which is much lower than that of the reference TPN-GDY under the same condition. Our results indicate that the strategy of adjusting the distribution of acetylenic bonds is a useful method to improve the performance of the carbon-based catalyst. More active sites can be exposed to the reaction surface and participate in the catalytic process. The as-prepared flexible TPM-GDY film has shown good potential for applications in the field of electrocatalyst devices, which inspires us to develop a general approach in the field of fabricating GDY-based electrocatalysts with high activity.

Conflicts of interest

There are no conflicts to declare.

Acknowledgements

The National Key Research and Development Project of China (2018YFA0703501), the National Natural Science Foundation of China (21875274), Young Scholarship Funding of Shandong University, and Taishan Scholars Youth Expert Program of Shandong Province (tsqn201909050).

References

1 H. Wang, Y. Shao, S. Mei, Y. Lu, M. Zhang, J.-k. Sun, K. Matyjaszewski, M. Antonietti and J. Yuan, Polymer-Derived Heteroatom-Doped Porous Carbon Materials, *Chem. Rev.*, 2020, **120**, 9363–9419.
2 T. Asefa, Metal-Free and Noble Metal-Free Heteroatom-Doped Nanostructured Carbons as Prospective Sustainable Electrocatalysts, *Acc. Chem. Res.*, 2016, **49**, 1873–1883.
3 Q. Wu, L. Yang, X. Wang and Z. Hu, From Carbon-Based Nanotubes to Nanocages for Advanced Energy Conversion and Storage, *Acc. Chem. Res.*, 2017, **50**, 435–444.
4 X. Deng, J. Li, L. Ma, J. Sha and N. Zhao, Three-Dimensional Porous Carbon Materials and Their Composites as Electrodes for Electrochemical Energy Storage Systems, *Mater. Chem. Front.*, 2019, **3**, 2221–2245.
5 W. Fan, L. Zhang and T. Liu, Multifunctional Second Barrier Layers for Lithium–Sulfur Batteries, *Mater. Chem. Front.*, 2018, **2**, 235–252.
6 Y. Jia, J. Chen and X. Yao, Defect Electrocatalytic Mechanism: Concept, Topological Structure and Perspective, *Mater. Chem. Front.*, 2018, **2**, 1250–1268.
7 J. Li, X. Gao, L. Zhu, M. N. Ghazzal, J. Zhang, C.-H. Tung and L.-Z. Wu, Graphdiyne for Crucial Gas Involved Catalytic Reactions in Energy Conversion Applications, *Energy Environ. Sci.*, 2020, **13**, 1326–1346.
8 J. Yu, G. Li, H. Liu, L. Zeng, L. Zhao, J. Jia, M. Zhang, W. Zhou, H. Liu and Y. Hu, Electrochemical Flocculation Integrated Hydrogen Evolution Reaction of Fe@N-Doped Carbon Nanotubes on Iron Foam for Ultralow Voltage Electrolysis in Neutral Media, *Adv. Sci.*, 2019, **6**, 1901458.
9 M.-S. Balogun, W. Qiu, H. Yang, W. Fan, Y. Huang, P. Fang, G. Li, H. Ji and Y. Tong, A Monolithic Metal-Free Electrocatalyst for Oxygen Evolution Reaction and Overall Water Splitting, *Energy Environ. Sci.*, 2016, **9**, 3411–3416.
10 K. Gong, F. Du, Z. Xia, M. Durstock and L. Dai, Nitrogen-Doped Carbon Nanotube Arrays with High Electrocatalytic Activity for Oxygen Reduction, *Science*, 2009, **323**, 760–764.
11 N. L. Yang, Y. Y. Liu, H. Wen, Z. Y. Tang, H. J. Zhao, Y. L. Li and D. Wang, Photocatalytic Properties of Graphdiyne and Graphene Modified TiO2: From Theory to Experiment, *ACS Nano*, 2013, **7**, 1504–1512.
12 K. Qu, Y. Zheng, X. Zhang, K. Davey, S. Dai and S. Z. Qiao, Promotion of Electrocatalytic Hydrogen Evolution Reaction on Nitrogen-Doped Carbon Nanosheets with Secondary Heteroatoms, *ACS Nano*, 2017, **11**, 7293–7300.
13 M. H. Naveen, K. Shim, M. S. A. Hossain, J. H. Kim and Y.-B. Shim, Template Free Preparation of Heteroatoms Doped Carbon Spheres with Trace Fe for Efficient Oxygen Reduction Reaction and Supercapacitor, *Adv. Energy Mater.*, 2017, **7**, 1602002.
14 J.-T. Ren, C.-Y. Wan, T.-Y. Pei, X.-W. Lv and Z.-Y. Yuan, Promotion of Electrocatalytic Nitrogen Reduction Reaction on N-doped Porous Carbon with Secondary Heteroatoms, *Appl. Catal., B*, 2020, **266**, 118633.
15 X. Yue, S. Huang, J. Cai, Y. Jin and P. K. Shen, Heteroatoms Dual Doped Porous Graphene Nanosheets as Efficient Bifunctional Metal-Free Electrocatalysts for Overall Water-Splitting, *J. Mater. Chem. A*, 2017, **5**, 7784–7790.
16 L. Lyu, K.-d. Seong, D. Ko, J. Choi, C. Lee, T. Hwang, Y. Cho, X. Jin, W. Zhang, H. Pang and Y. Piao, Recent Development of Biomass-Derived Carbons and Composites as Electrode

Materials for Supercapacitors, *Mater. Chem. Front.*, 2019, **3**, 2543–2570.

17 L. Oar-Arteta, T. Wezendonk, X. Sun, F. Kapteijn and J. Gascon, Metal Organic Frameworks as Precursors for the Manufacture of Advanced Catalytic Materials, *Mater. Chem. Front.*, 2017, **1**, 1709–1745.

18 X. Wang, L. Liu and Z. Niu, Carbon-Based Materials for Lithium-Ion Capacitors, *Mater. Chem. Front.*, 2019, **3**, 1265–1279.

19 L. Xie, F. Su, L. Xie, X. Guo, Z. Wang, Q. Kong, G. Sun, A. Ahmad, X. Li, Z. Yi and C. Chen, Effect of Pore Structure and Doping Species on Charge Storage Mechanisms in Porous Carbon-Based Supercapacitors, *Mater. Chem. Front.*, 2020, **4**, 2610–2634.

20 Z. W. Seh, J. Kibsgaard, C. F. Dickens, I. B. Chorkendorff, J. K. Norskov and T. F. Jaramillo, Combining Theory and Experiment in Electrocatalysis: Insights into Materials Design, *Science*, 2017, **355**, eaad4998.

21 D. Guo, H.-F. Wei, R.-B. Song, J. Fu, X. Lu, R. Jelinek, Q. Min, J.-R. Zhang, Q. Zhang and J.-J. Zhu, N,S-Doped Carbon Dots as Dual-Functional Modifiers to Boost Bio-Electricity Generation of Individually-Modified Bacterial Cells, *Nano Energy*, 2019, **63**, 103875.

22 Q. Zhang, Z. Zhou, Z. Pan, J. Sun, B. He, Q. Li, T. Zhang, J. Zhao, L. Tang, Z. Zhang, L. Wei and Y. Yao, All-Metal-Organic Framework-Derived Battery Materials on Carbon Nanotube Fibers for Wearable Energy-Storage Device, *Adv. Sci.*, 2018, **5**, 1801462.

23 G. Li, Y. Li, H. Liu, Y. Guo, Y. Li and D. Zhu, Architecture of Graphdiyne Nanoscale Films, *Chem. Commun.*, 2010, **46**, 3256–3258.

24 Z. Y. Jia, Y. J. Li, Z. C. Zuo, H. B. Liu, C. S. Huang and Y. L. Li, Synthesis and Properties of 2D Carbon-Graphdiyne, *Acc. Chem. Res.*, 2017, **50**, 2470–2478.

25 C. Huang, Y. Li, N. Wang, Y. Xue, Z. Zuo, H. Liu and Y. Li, Progress in Research into 2D Graphdiyne-Based Materials, *Chem. Rev.*, 2018, **118**, 7744–7803.

26 Y. Li, L. Xu, H. Liu and Y. Li, Graphdiyne and Graphyne: From Theoretical Predictions to Practical Construction, *Chem. Soc. Rev.*, 2014, **43**, 2572–2586.

27 H. Yu, Y. Xue and Y. Li, Graphdiyne and its Assembly Architectures: Synthesis, Functionalization, and Applications, *Adv. Mater.*, 2019, **31**, 1803101.

28 L. Gao, X. Ge, Z. Zuo, F. Wang, X. Liu, M. Lv, S. Shi, L. Xu, T. Liu, Q. Zhou, X. Ye and S. Xiao, High Quality Pyrazinoquinoxaline-Based Graphdiyne for Efficient Gradient Storage of Lithium Ions, *Nano Lett.*, 2020, **20**, 7333–7341.

29 J. Li, M. Zhao, C. Zhao, H. Jian, N. Wang, L. Yao, C. Huang, Y. Zhao and T. Jiu, Graphdiyne-Doped P3CT-K as an Efficient Hole-Transport Layer for MAPbI(3) Perovskite Solar Cells, *ACS Appl. Mater. Interfaces*, 2019, **11**, 2626–2631.

30 M. Long, L. Tang, D. Wang, Y. Li and Z. Shuai, Electronic Structure and Carrier Mobility in Graphdiyne Sheet and Nanoribbons: Theoretical Predictions, *ACS Nano*, 2011, **5**, 2593–2600.

31 L. Hui, Y. Xue, H. Yu, Y. Liu, Y. Fang, C. Xing, B. Huang and Y. Li, Highly Efficient and Selective Generation of Ammonia and Hydrogen on a Graphdiyne-Based Catalyst, *J. Am. Chem. Soc.*, 2019, **141**, 10677–10683.

32 Y. Xue, B. Huang, Y. Yi, Y. Guo, Z. Zuo, Y. Li, Z. Jia, H. Liu and Y. Li, Anchoring Zero Valence Single Atoms of Nickel and Iron on Graphdiyne for Hydrogen Evolution, *Nat. Commun.*, 2018, **9**, 1460.

33 Y. Xue, Z. Zuo, Y. Li, H. Liu and Y. Li, Graphdiyne-Supported $NiCo_2S_4$ Nanowires: A Highly Active and Stable 3D Bifunctional Electrode Material, *Small*, 2017, **13**, 1700936.

34 H. Yu, Y. Xue, L. Hui, C. Zhang, Y. Zhao, Z. Li and Y. Li, Controlled Growth of MoS_2 Nanosheets on 2D N-Doped Graphdiyne Nanolayers for Highly Associated Effects on Water Reduction, *Adv. Funct. Mater.*, 2018, **28**, 1707564.

35 N. Wang, J. He, Z. Tu, Z. Yang, F. Zhao, X. Li, C. Huang, K. Wang, T. Jiu, Y. Yi and Y. Li, Synthesis of Chlorine-Substituted Graphdiyne and Applications for Lithium-Ion Storage, *Angew. Chem., Int. Ed.*, 2017, **56**, 10740–10745.

36 N. Wang, X. Li, Z. Tu, F. Zhao, J. He, Z. Guan, C. Huang, Y. Yi and Y. Li, Synthesis and Electronic Structure of Boron-Graphdiyne with an sp-Hybridized Carbon Skeleton and Its Application in Sodium Storage, *Angew. Chem., Int. Ed.*, 2018, **57**, 3968–3973.

37 C. Xing, Y. Xue, B. Huang, H. Yu, L. Hui, Y. Fang, Y. Liu, Y. Zhao, Z. Li and Y. Li, Fluorographdiyne: A Metal-Free Catalyst for Applications in Water Reduction and Oxidation, *Angew. Chem., Int. Ed.*, 2019, **58**, 13897–13903.

38 R. Sakamoto, R. Shiotsuki, K. Wada, N. Fukui, H. Maeda, J. Komeda, R. Sekine, K. Harano and H. Nishihara, A Pyrazine-Incorporated Graphdiyne Nanofilm as a Metal-Free Electrocatalyst for the Hydrogen Evolution Reaction, *J. Mater. Chem. A*, 2018, **6**, 22189–22194.

39 Y. Du, W. Zhou, J. Gao, X. Pan and Y. Li, Fundament and Application of Graphdiyne in Electrochemical Energy, *Acc. Chem. Res.*, 2020, **53**, 459–469.

40 J. Zhou, X. Gao, R. Liu, Z. Xie, J. Yang, S. Zhang, G. Zhang, H. Liu, Y. Li, J. Zhang and Z. Liu, Synthesis of Graphdiyne Nanowalls Using Acetylenic Coupling Reaction, *J. Am. Chem. Soc.*, 2015, **137**, 7596–7599.

41 G. Abdi, A. Filip, M. Krajewski, K. Kazimierczuk, M. Strawski, P. Szarek, B. Hamankiewicz, Z. Mazej, G. Cichowicz, P. J. Leszczynski, K. J. Fijalkowski and A. Szczurek, Toward the Synthesis, Fluorination and Application of N-Graphyne, *RSC Adv.*, 2020, **10**, 40019–40029.

42 F. He, C. Xing and Y. Xue, Metal-Free Amino-Graphdiyne for Applications in Electrocatalytic Hydrogen Evolution, *J. Catal.*, 2021, **395**, 129–135.

43 H. Yu, Y. Xue, L. Hui, F. He, C. Zhang, Y. Liu, Y. Fang, C. Xiang, Y. Li, H. Liu and Y. Li, Graphdiyne-Engineered Heterostructures for Efficient Overall Water-Splitting, *Nano Energy*, 2019, **64**, 103928.

44 W. Guo, E. Galoppini, R. Gilardi, G. I. Rydja and Y.-H. Chen, Weak Intermolecular Interactions in the Crystal Structures of Molecules with Tetrahedral Symmetry: Diamondoid Nets and Other Motifs, *Cryst. Growth Des.*, 2001, **1**, 231–237.

45 C. Y. Wu, Y. M. Liu, H. Liu, C. H. Duan, Q. Y. Pan, J. Zhu, F. Hu, X. Y. Ma, T. G. Jiu, Z. B. Li and Y. J. Zhao, Highly

Conjugated Three-Dimensional Covalent Organic Frameworks Based on Spirobifluorene for Perovskite Solar Cell Enhancement, *J. Am. Chem. Soc.*, 2018, **140**, 10016–10024.

46 H. Yu, Y. Xue, L. Hui, C. Zhang, Y. Zhao, Z. Li and Y. Li, Controlled Growth of MoS_2 Nanosheets on 2D N-Doped Graphdiyne Nanolayers for Highly Associated Effects on Water Reduction, *Adv. Funct. Mater.*, 2018, 28.

47 X. Kan, D. Wang, Q. Pan, Y. Wang, Y. Xiao, J. Liu, Y. Zhao and Z. Li, Confined Interfacial Synthesis of Highly Crystalline and Ultrathin Graphdiyne Films and Their Applications for N-2 Fixation, *Chem. – Eur. J.*, 2020, **26**, 7801–7807.

48 W. X. Zhou, H. Shen, Y. Zeng, Y. P. Yi, Z. C. Zuo, Y. J. Li and Y. L. Li, Controllable Synthesis of Graphdiyne Nanoribbons, *Angew. Chem., Int. Ed.*, 2020, **59**, 4908–4913.

49 C. Xie, X. Hu, Z. Guan, X. Li, F. Zhao, Y. Song, Y. Li, X. Li, N. Wang and C. Huang, Tuning the Properties of Graphdiyne by Introducing Electron-Withdrawing/Donating Groups, *Angew. Chem., Int. Ed.*, 2020, **59**, 13542–13546.

50 J. He, N. Wang, Z. Yang, X. Shen, K. Wang, C. Huang, Y. Yi, Z. Tu and Y. Li, Fluoride Graphdiyne as a Free-Standing Electrode Displaying Ultra-Stable and Extraordinary High Li Storage Performance, *Energy Environ. Sci.*, 2018, **11**, 2893–2903.

51 A. Degli Esposti, V. Fattori, C. Sabatini, G. Casalbore-Miceli and G. Marconi, The Electron Transfer Rate of Large TPA Based Compounds: a Joint Theoretical and Electrochemical Approach, *Phys. Chem. Chem. Phys.*, 2005, **7**, 3738–3743.

52 J. Guo, M. Y. Guo, F. H. Wang, W. Y. Jin, C. Y. Chen, H. B. Liu and Y. L. Li, Graphdiyne:Structure of Fluorescent Quantum Dots, *Angew. Chem., Int. Ed.*, 2020, **59**, 16712–16716.

53 Y. Xue, J. Li, Z. Xue, Y. Li, H. Liu, D. Li, W. Yang and Y. Li, Extraordinarily Durable Graphdiyne-Supported Electrocatalyst with High Activity for Hydrogen Production at All Values of pH, *ACS Appl. Mater. Interfaces*, 2016, **8**, 31083–31091.

54 T. Lu, J. He, R. Li, K. Wang, Z. Yang, X. Shen, Y. Li, J. Xiao and C. Huang, Adjusting the Interface Structure of Graphdiyne by H and F Co-Doping for Enhanced Capacity and Stability in Li-ion Battery, *Energy Storage Mater.*, 2020, **29**, 131–139.

55 C. Lu, Y. Yang, J. Wang, R. P. Fu, X. X. Zhao, L. Zhao, Y. Ming, Y. Hu, H. Z. Lin, X. M. Tao, Y. L. Li and W. Chen, High-Performance Graphdiyne-Based Electrochemical Actuators, *Nat. Commun.*, 2018, **9**, 752.

56 S. Zhuo, Y. Shi, L. Liu, R. Li, L. Shi, D. H. Anjum, Y. Han and P. Wang, Dual-Template Engineering of Triple-Layered Nanoarray Electrode of Metal Chalcogenides Sandwiched with Hydrogen-Substituted Graphdiyne, *Nat. Commun.*, 2018, **9**, 3132.

57 J. Balamurugan, N. Thanh Tuan, V. Aravindan, N. H. Kim and J. H. Lee, Flexible Solid-State Asymmetric Supercapacitors Based on Nitrogen-Doped Graphene Encapsulated Ternary Metal-Nitrides with Ultralong Cycle Life, *Adv. Funct. Mater.*, 2018, **28**, 1804663.

58 Q. Lv, N. Wang, W. Si, Z. Hou, X. Li, X. Wang, F. Zhao, Z. Yang, Y. Zhang and C. Huang, Pyridinic Nitrogen Exclusively Doped Carbon Materials as Efficient Oxygen Reduction Electrocatalysts for Zn-Air Batteries, *Appl. Catal., B*, 2020, **261**, 118234.

59 X. Shen, J. He, K. Wang, X. Li, X. Wang, Z. Yang, N. Wang, Y. Zhang and C. Huang, Fluorine-Enriched Graphdiyne as an Efficient Anode in Lithium-Ion Capacitors, *ChemSusChem*, 2019, **12**, 1342–1348.

60 J. He, N. Wang, Z. Cui, H. Du, L. Fu, C. Huang, Z. Yang, X. Shen, Y. Yi, Z. Tu and Y. Li, Hydrogen Substituted Graphdiyne as Carbon-Rich Flexible Electrode for Lithium and Sodium Ion Batteries, *Nat. Commun.*, 2017, **8**, 1172.

61 L. Hui, Y. Xue, B. Huang, H. Yu, C. Zhang, D. Zhang, D. Jia, Y. Zhao, Y. Li, H. Liu and Y. Li, Overall Water Splitting by Graphdiyne-Exfoliated and -Sandwiched Layered Double-Hydroxide Nanosheet Arrays, *Nat. Commun.*, 2018, **9**, 5309.

62 Y. Fang, Y. Xue, L. Hui, H. Yu, Y. Liu, C. Xing, F. Lu, F. He, H. Liu and Y. Li, In Situ Growth of Graphdiyne Based Heterostructure: Toward Efficient Overall Water Splitting, *Nano Energy*, 2019, **59**, 591–597.

